Department of Advanced Materials Science
Graduate School of Frontier Science
The University of Tokyo

2008

Master's Thesis

Electrical Properties of Oxide Junctions under Light Irradiation

(酸化物を用いた接合における光照射下での電気特性)

Submitted on January 29th, 2008
Supervisor : Associate Professor Harold Y. Hwang 黄

66134: Motoshi Nakayama

Contents

Chapter 1

General introduction

1.1 Oxides as correlated electron systems

According to the classification of insulators, there are two basic categories of insulators. First is the insulators due to the electron-ion interaction and the second is the insulators due to the electron-electron interaction. The first class is further divided into the following three classes, band insulators, Peierls insulators and Anderson insulators. Band insulators are insulators due to the interaction of the electron and the periodic potential of the ions, Peierls insulators are insulators due to the interaction of the electron and the lattice deformation, and Anderson insulators are the insulators due to the interaction with the electron and the impurities and the imperfection of the lattice [1].

The other category of insulators is called Mott insulators. Historically, Verwey and de Boer indicated that transition metal oxides such as NiO and CoO exhibit poor conductivity even though the bands derived from the $3d$ orbitals of the transition metals are not filled [2]. After the theoretical studies, it was realized that localization of the d-electrons and the splitting of d-bands are induced by the electron-electron interaction. Transition metal oxides are for that reason attractive material series to study the electron correlation and indeed much attention has been paid for the study of these materials.

One of the characteristics of the Mott insulators is that they show high resistivity even at high doping levels. For instance, $LaTiO_3$ shows high resistivity even though the carrier density is more than 10^{22} cm^{-3} [3], although Si shows a metal insulator transition at 4×10^{18} cm^{-3} [4]. Another characteristic is that the band picture with a one electron approximation is not applicable and the band structure changes with the doping level.

Transition metal oxides sometimes show dramatic change in the physical properties, such as superconducting transition at high temperature in cuprates, and colossal magnetoresistance in manganite with carrier doping level, and with external field such as temperature, magnetic field and light. These properties also attract us for the study of oxides.

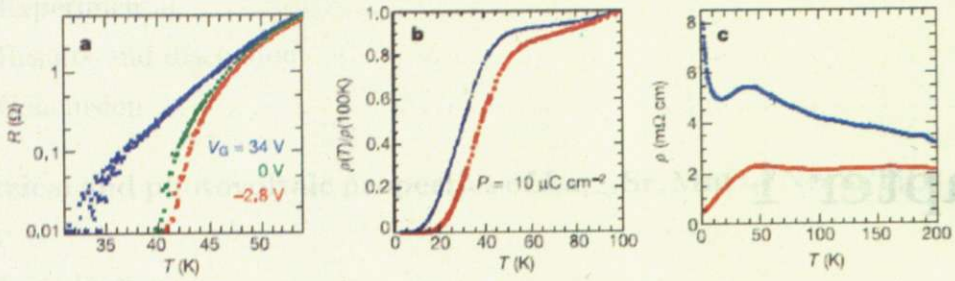

Figure 1.1: Examples of carrier density modulation by electric field: (a) resistivity change of a $YBa_2Cu_3O_7$ channel with $Ba_{0.15}Sr_{0.85}TiO_3$ gate insulator [5] and (b), (c) Resistance changes at different doping levels of $GdBa_2CuO_{7-x}$ films with PZT ferroelectric gates [6]. Figure is from [7].

1.2 Carrier doping using heterointerfaces

The usual method of carrier doping in oxides is chemical substitution of atoms. In the case of compounds with the perovskite type structure, it has the general formula ABO_3, where A is often a trivalent rare earth such as La or divalent alkali rare earth such as Sr, Ca, and B is a transition metal. By changing the composition of the trivalent and the divalent atoms at the A site, carrier doping levels in the d orbitals of the B site transition metal changes. This method is quite useful to control the carrier density, but the modification of the composition induces lattice distortion consequence. If we go back to the theory of correlated electron systems, this system is most simply explained with in the Hubbard model,

$$H = -t\Sigma a_{i+1}^{\dagger} a_i + U\Sigma n_{i\uparrow} n_{i\downarrow} \tag{1.1}$$

where the first term on the right side represents transfer to neighboring sites, and the second term represents the on site Coulomb repulsion. t and U corresponds to the energy to move to the neighbor site (transfer integral) and on site Coulomb repulsion, respectively. Physical states in correlated electron systems are parametrized with the ratio U/t, which is affected by lattice distortions and the carrier density n, so carrier doping with chemical substitution is sometimes undesirable to control only n.

With the progress in the techniques to fabricate high quality interfaces between oxides or oxides and metals, it has become popular to investigate the physical states with the method to dope carriers using interface structures. One such method is electric field modulation using the field effect transistor (FET) structure (Fig. 1.1) [5, 6]. Photocarrier injection is another approach. Suppose an abrupt p^+-n heterojunction forms with oxides as shown in Fig. 1.2. Holes are injected from the right to the left by the internal electric field at the interface immediately after the light is irradiated, although electrons cannot be injected because of the high conduction band offset seen from the right. This can be

regarded as hole doping to the oxides on the left. Katsu *et al.* reported photocarrier injection in $La_{1-x}Sr_xMnO_3$ in the structure $La_{1-x}Sr_xMnO_3/SrTiO_3$ and they observed change in magnetization [8]. Muraoka *et al.* observed the change of the superconducting T_c in the $YBa_2Cu_3O_7/Nb : SrTiO_3$ under light irradiation (Fig. 1.3) [9].

Advantages of these methods are the tunability of the doping level and doping without chemical substitution. These methods enable us to study the behavior near the transition, and to examine complete filling control. However there are several unclear points remaining. For example, give the band alignment between correlated electrons systems, for which the band structure can be changed with the doping level, the doping level are not obvious. It is also not obvious whether doping level is sufficient for the modulation of physical properties of correlated oxides.

1.3 Aim and scope of this thesis

In this thesis, we focus on the electronic properties of oxide junctions under light irradiation in order to gain further insights for the photocarrier injection method. As a model system, we use junctions with $SrTiO_3$, which is commercially available as single crystal substrates and lattice matched to many perovskites showing fascinating physical properties. In the following chapter, we will discuss the basics to understand the electric properties of junctions, especially Schottky junctions and their photovoltaic properties. In Chapter 3, we briefly review the electrical properties of $Au/Nb : SrTiO_3$ junctions. In Chapter 4, we study the electric properties of $Au/SrTiO_3$ junctions under UV irradiation, in order to understand the junction properties for a conventional metal and "photo-doped" $SrTiO_3$ junction, as well as the photoirradiation effects on the junction properties. In Chapter 5, the photovoltaic properties with $Au/Nb : SrTiO_3$ junctions are studied from the viewpoint of the efficiency of photocarrier injection. Finally the photovoltaic properties of $La_{1-x}Sr_xMnO_3/Nb : SrTiO_3$ junctions are studied in Chapter 6 as one case of an oxide heterostructure from the viewpoint of photocarrier injection into correlated oxides.

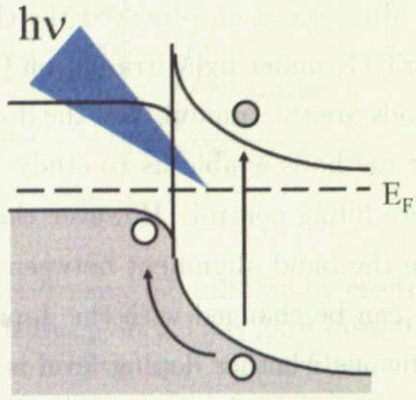

Figure 1.2: Schematic diagram of photocarrier injection. photo-generated holes in the oxide on the right are selectively injected to the oxide on the left.

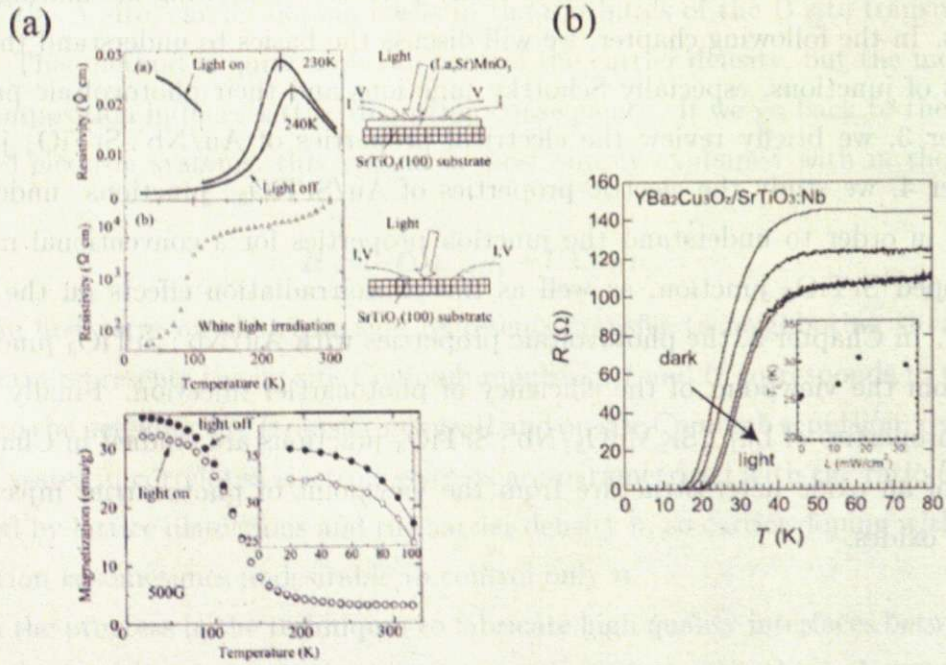

Figure 1.3: Examples of photocarrier injection in transition metal oxides: (a) Temperature dependent resistivity and magnetization of a $La_{1-x}Sr_xMnO_3$ film on $SrTiO_3$ is modified by light irradiation [8] and (b) T_c of $YBa_2Cu_3O_7/Nb : SrTiO_3$ is controlled by light irradiation [9].

Chapter 2

Basic theory of interfaces

In this chapter, we will discuss the basic theory of the physical properties of junctions and that of solar cells, and photovoltaic properties according to the study of conventional semiconductors [10]. We will also discuss the principles of measurement in the open circuit photovoltage decay to obtain the lifetime of injected carriers, which is one of the characteristic parameters of photovoltaic properties.

2.1 Schottky junctions

2.1.1 Formation of Schottky junction

When two materials are attached chemically, interesting behaviors are observed at the interface due to the asymmetric nature of the physical properties at the interface. The most interesting property is rectifying behavior, and electronic devices using this behavior such as transistors and diodes are the key devices of today's electronics.

When a p-type semiconductor makes contact with an n-type semiconductor, a p-n junction is formed after electrons in the n-type semiconductor and the holes in the p-type semiconductor diffuse across the interface. When a metal and a semiconductor makes contact, a Schottky junction is formed at the interface. Fig. 2.1 shows the the schematic band diagram of a metal and an n-type semiconductor contact. The band diagram of the metal and the n-type semiconductor at thermal equilibrium is shown in Fig. 2.1 (a). When the metal and the semiconductor is attached, electrons diffuse from the semiconductor to the metal to establish thermal equilibrium at the interface. Fermi levels of the metal and the semiconductor coincide, and as a result, a potential barrier called the Schottky barrier is formed at the interface. The Schottky barrier height $q\phi_{bn}$ is expressed as the difference between the work function of the metal, $q\phi_m$, and the electron affinity of the semiconductor, χ, as follows,

$$q\phi_{bn} = q(\phi_m - \chi). \tag{2.1}$$

The height of the barrier from the bottom of the conduction band in the semiconductor

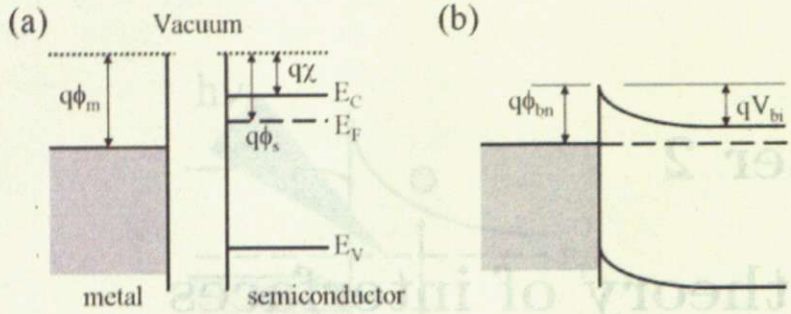

Figure 2.1: Band diagrams of metal-semiconductor contacts: (a) before making contact and (b) the formation of a Schottky junction after making contact.

is called the built-in potential, V_{bi} and is given by,

$$qV_{bi} = q(\phi_m - \phi_s) \tag{2.2}$$

where $q\phi_s$ is the work function of the semiconductor. We call this model to describe the Schottky barrier height formation as the Schottky-Mott model.

2.1.2 Depletion layer

In equilibrium, some electrons in the semiconductor diffuse to the metal, so there is a region where electrons are absent. We call this region the depletion layer. If the carrier density of the n-type semiconductor is N_D, only fixed positive charges are distributed with the density of N_D in the depletion layer (Fig. 2.2 (a)). Poisson's equation can be written as,

$$\frac{d^2V(x)}{dx^2} = -\frac{\rho(x)}{\epsilon_s} \tag{2.3}$$

where ϵ_s is permittivity of the semiconductor, $\rho(x) \simeq qN_D$ $(0 \leq x \leq W)$ and $\rho(x) \simeq 0$ $(x > W)$, and W is the depletion width. By solving the equation with the boundary condition, $V = V_{bi}$ at $x = 0$ and $V = 0$ at $x = W$, we obtain the depletion layer width as

$$W = \sqrt{\frac{2\epsilon_s(V_{bi} - V)}{qN_D}}. \tag{2.4}$$

The electric field and the potential are given by,

$$|E(x)| = \frac{qN_D}{\epsilon_s}(W - x) \tag{2.5}$$

and

$$V(x) = \frac{qN_D}{\epsilon_s}(Wx - \frac{1}{2}x^2) - \phi_{bn}. \tag{2.6}$$

The distribution of the electric field and the potential are shown in Fig. 2.2 (b) and (c).

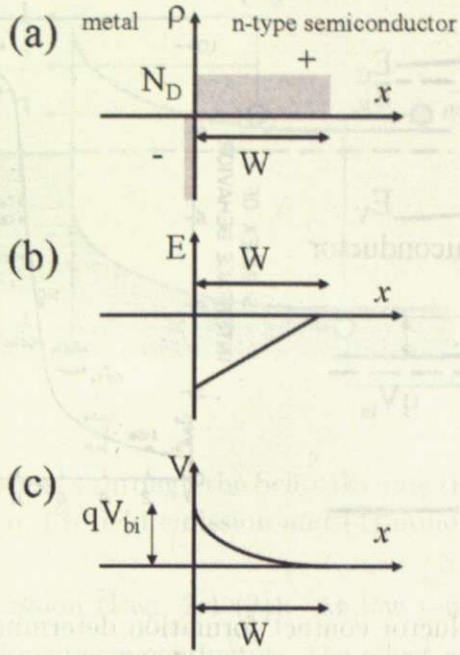

Figure 2.2: : Thermal equilibrium of the Schottky junction. (a) Space-charge distribution. (b) Electric field distribution. (c) Potential variation with distance.

The charge depleted region in the semiconductor acts as a capacitor called depletion layer capacitance , which is defined as $C \equiv dQ_{sc}/dV$, where $Q_{sc} = qN_DW$, so the depletion layer capacitance per unit area in the Schottky junction is given by,

$$C = \frac{|\partial Q_{sc}|}{\partial V} = \sqrt{2q\epsilon_s N_D(V_{bi} - V)} = \frac{\epsilon_s}{W}. \tag{2.7}$$

2.1.3 Surface states

In ideal conditions, the Schottky barrier height is described with Eq. 2.1, but in reality, electronic states are formed within the energy gap of semiconductors because of the dangling bonds or the sudden termination of the periodic lattice structure at the surface. Such states are called surface states and this causes the bending of the energy band near the surface to establish equilibrium (Fig. 2.3 (a)). In this case, the barrier is also formed when the semiconductor and the metal are making contact, however, the barrier height is not described by Eq. 2.1, but by the charge neutrality of the surface states and the space charge in the semiconductor (Fig. 2.3 (b)). We call such for the barrier height as the Bardeen model.

For example, junctions between a metal and a "covalent" semiconductor such as Si or GaAs, the junction formation is well described by the Bardeen model and the barrier height is essentially independent of the metal work function. On the other hand, in

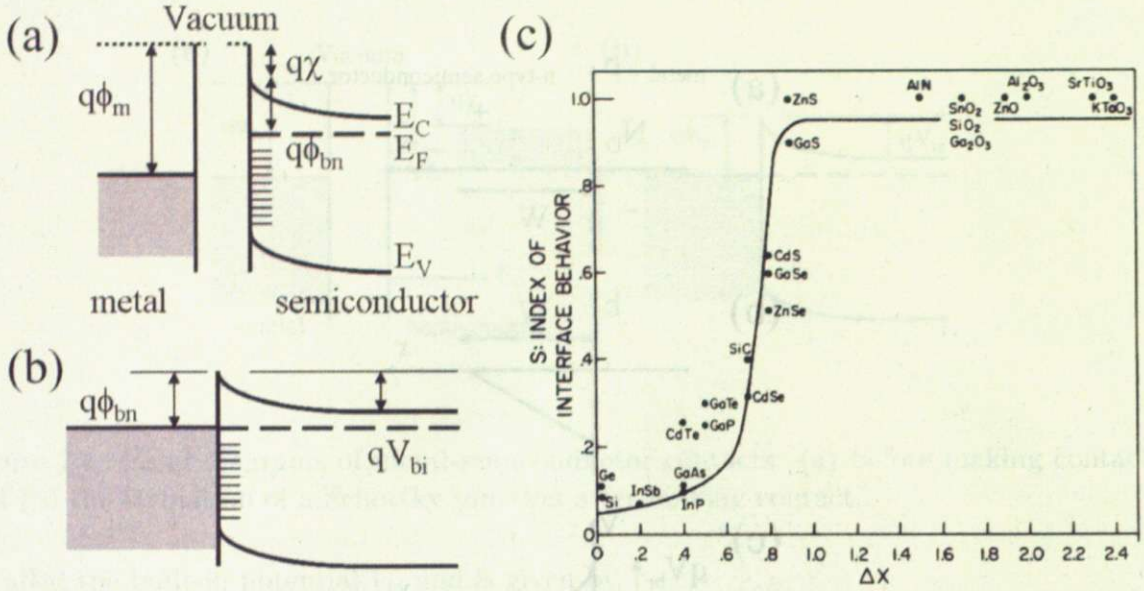

Figure 2.3: Metal-semiconductor contact formation determined by surface states in the semiconductor: (a) before making contact and (b) after making contact. (c) S as a function of electronegativity difference in the semiconductors [11].

the case of a junction between a metal and an "ionic" semiconductor, a junction forms following the Schottky-Mott model and the barrier height depends strongly on the work function of the metal. A parameter to characterize the ionicity of the compounds is the the difference in electronegativity (X) of the constituents of semiconductors (ΔX). If we define a parameter S as

$$S \equiv \frac{d\phi_{bn}}{dX_M} \tag{2.8}$$

where X_M is the electronegativity of the metal, the relationship between the ionicity of semiconductors and S is plotted in Fig. 2.3 (c) [11]. From this figure, as long as ΔX of a semiconductor is more than 1, the Schottky-Mott model is thought to be applicable.

2.1.4 Transport property of the Schottky junction

As we mentioned before, the most important property of Schottky junctions is the rectifying behavior, so in this part we discuss the transport property of the junction. The current transport is mainly due to the majority carriers (electrons, in the case of a junction with a metal and an n-type semiconductor). Figure 2.4 shows basic current transport processes through the junction. The current transport carried out by majority carriers which have the energy to overcome the Schottky barrier is the most basic process and it is called thermionic emission (Fig. 2.4 (1)). Other basic processes are caused by quantum mechanical tunneling through the barrier. If carriers tunnel with the assistance of thermal energy, it is called thermionic-field emission (Fig. 2.4 (2)), and transport caused by direct

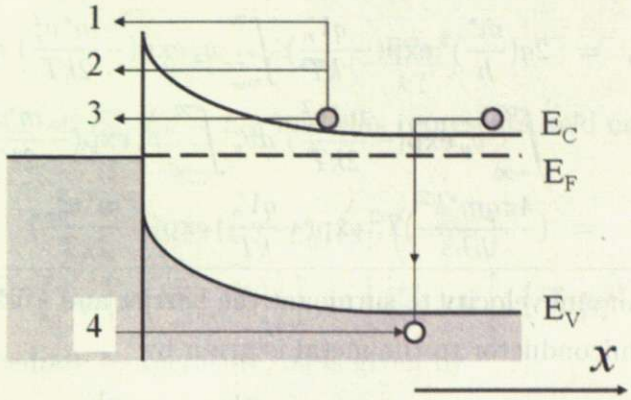

Figure 2.4: The current processes through the Schottky junction: (1) thermionic emission, (2) thermionic-field emission, (3) field emission and (4) minority carrier injection.

tunneling is called field emission (Fig. 2.4 (3)). At low temperatures or in the case of the junction with heavily doped semiconductors, the effect of tunneling is nonnegligible. The current process caused by minority carriers injected from the metal is also one of the basic current processes (Fig. 2.4 (4)).

We discuss the thermionic emission property analytically. First we assume (1) the barrier height is sufficiently larger than the thermal energy ($q\phi_{bn} >$ kT, where k is the Boltzmann constant), (2) thermal equilibrium is established, and (3) the current flow does not affect thermal equilibrium. The current flow in the x direction from the semiconductor to the metal $J_{s\to m}$ is given by

$$J_{s\to m} = \int_{q\phi_{bn}+E_F}^{\infty} q v_x \, dn \tag{2.9}$$

where $q\phi_{bn} + E_F$ is the minimum energy for thermionic emission and v_x is the velocity of an electron in x direction. The electron density in unit energy range dn is given by

$$\begin{aligned} dn &= N(E)F(E)\, dE & (2.10)\\ &= \frac{4\pi(2m^*)^{3/2}}{h^3}\sqrt{E-E_C}\exp[-(E-E_C+qV_n)/kT]\, dE & (2.11)\end{aligned}$$

where $N(E)$ and $F(E)$ are the density of states and the Fermi-Dirac distribution function, m^* is the effective electron mass of the semiconductor, and qV_n is the energy difference between the conduction band and the Fermi level in the semiconductor, $E_C - E_F$. With the relation $E_C - E = \frac{1}{2}m^*v^2$, Eq. 2.11 gives

$$dn = 2(\frac{m^*}{h})^3 \exp(-\frac{m^*v^2}{2kT})(4\pi v^2\, dv). \tag{2.12}$$

$v^2 = v_x^2 + v_y^2 + v_z^2$ and $4\pi v^2 dv = dv_x dv_y dv_z$, so we obtain

$$J_{s\to m} = 2q(\frac{m^*}{h})^3 \exp(-\frac{qV_n}{kT}) \int_{v_{0x}}^{\infty} v_x \exp(-\frac{m^* v_x^2}{2kT})\, dv_x \tag{2.13}$$

$$\int_{-\infty}^{\infty} v_y \exp(-\frac{m^* v_y^2}{2kT})\, dv_y \int_{-\infty}^{\infty} v_z \exp(-\frac{m^* v_z^2}{2kT})\, dv_z \tag{2.14}$$

$$= (\frac{4\pi q m^* k^2}{h^3}) T^2 \exp(-\frac{qV_n}{kT}) \exp(-\frac{m^* v_{0x}^2}{2kT}) \tag{2.15}$$

where v_{0x} is the minimum velocity to surmount the barrier and $\frac{1}{2}m^* v_{0x} = q(V_{bi} - V)$. The current from the semiconductor to the metal is given by

$$J_{s\to m} = A^* T^2 \exp(-\frac{q\phi_{bn}}{kT}) \exp(\frac{qV}{kT}) \tag{2.16}$$

and

$$A^* = \frac{4\pi m^* k^2}{h^3} \tag{2.17}$$

is called the effective Richardson constant for thermionic emission.

Next, we discuss the current from the metal to the semiconductor. The barrier height from the metal Fermi level is independent of applied bias voltage, so the current is also independent of bias voltage. Furthermore, the total current must be zero at $V = 0$, so the current is given by

$$J_{m\to s} = -A^* T^2 \exp(-\frac{q\phi_{bn}}{kT}). \tag{2.18}$$

The total current for the thermionic emission (J_{tot}) is given by

$$J_{tot} = J_{s\to m} - J_{m\to s} = A^* T^2 \exp(-\frac{q\phi_{bn}}{kT})[\exp(\frac{qV}{kT}) - 1]. \tag{2.19}$$

However, ideal characteristics are difficult to observe because of the existence of current processes other than thermionic emission, so Eq. 2.19 is extended as

$$J_{tot} = A^* T^2 \exp(-\frac{q\phi_{bn}}{kT})[\exp(\frac{qV}{nkT}) - 1] \tag{2.20}$$

where n is called the ideality factor. For example, if electron-hole recombination current in the depletion region is dominating, n is equal to 2.

According to Padovani and Stratton [12], thermionic emission, thermionic-field emission, and field emission are expressed in identical formula,

$$J = J_0 \exp(\frac{qV}{E_0})[1 - \exp(-\frac{qV}{kT})] \tag{2.21}$$

where the parameter E_0 and the saturation current density J_0 are defined separately for each process.

$$E_0 = E_{00} \coth(\frac{E_{00}}{kT}) \tag{2.22}$$

$$E_{00} = \frac{hq}{4\pi}(\frac{N_D}{m^* \epsilon_s})^{1/2}. \tag{2.23}$$

If $kT \gg E_{00}$, $E_0 \simeq kT$, this represents thermionic emission and Eq. 2.21 reduces to Eq. 2.19 with

$$J_0 = A^* T^2 \exp(-\frac{q\phi_{bn}}{kT}). \tag{2.24}$$

At low temperature, $kT \ll E_0$, $E_0 = E_{00}$ and this represents field emission. In this case, J_0 is given by

$$J_0 = \frac{2\pi A^* T^2 E_{00} \exp\left(-\frac{q\phi_{bn}}{E_{00}}\right)}{kT\left\{\log\left[4\left(\frac{q\phi_{bn}-qV}{-qV_n}\right)\right]\right\}\sin\left\{\frac{\pi kT}{2E_{00}}\log\left[4\left(\frac{q\phi_{bn}-qV}{-qV_n}\right)\right]\right\}}. \tag{2.25}$$

In addition, at intermediate temperature, J_0 is given by

$$J_0 = \frac{A^* T^2 \pi^{1/2} E_{00}^{1/2} (q\phi_{bn} - qV - qV_n)^{1/2} \exp\left(\frac{-qV_n}{kT} - \frac{qV - qV_n}{E_0}\right)}{kT \coth(\frac{E_{00}}{kT})} \tag{2.26}$$

and this represents thermionic-field emission. Figure (2.5) shows the I-V characteristics of a Au/GaAs Schottky junction (a) and E_0 as a function of kT/q (b). As long as the current process follows thermionic emission, thermionic-field emission, or field emission, E_0 of the junction is well matched with the theoretical temperature dependence.

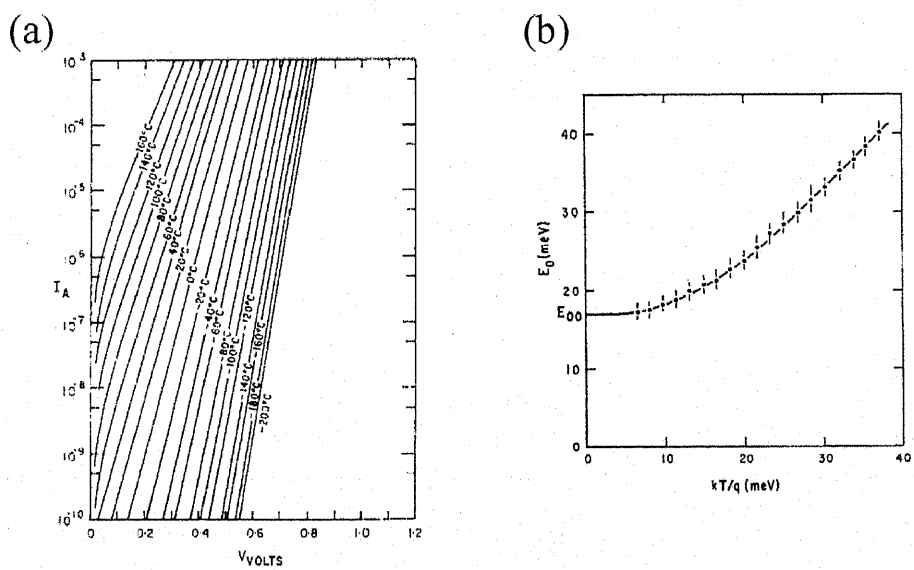

Figure 2.5: (a) I-V characteristics of a Au/GaAs Schottky junction and (b) temperature dependence of E_0 [12].

2.2 Photovoltaic effects

2.2.1 Basics of solar cells

The solar cell was first developed by Chapin *et al.* using a silicon p-n junction [13]. The basic mechanism of a solar cell is as follows. When light with energy larger than the band

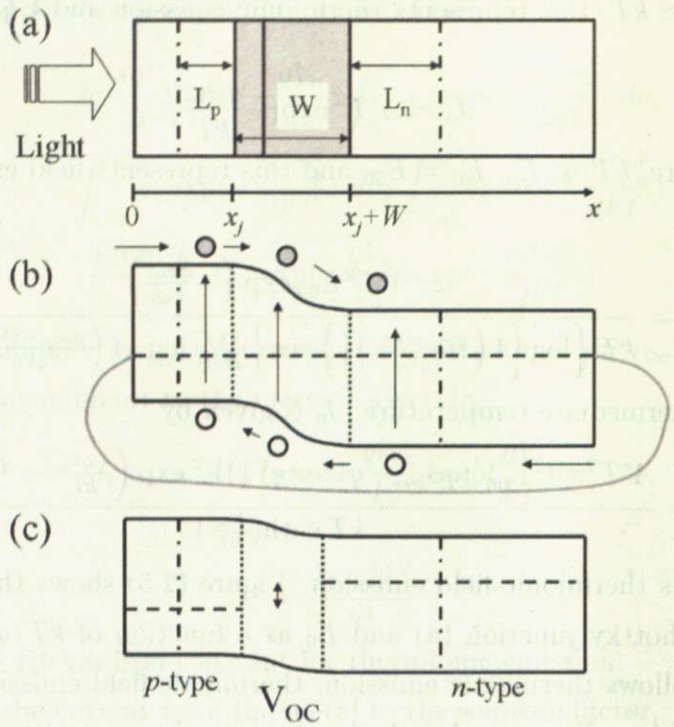

Figure 2.6: (a) Schematic picture of a p-n solar cell. (b) Band diagram in the short circuit condition. (c) Band diagram in the open circuit condition.

gap of a semiconductor is irradiated from the p-type semiconductor side as shown in Fig. 2.6, photons are absorbed and electrons and holes are generated. The distribution of the number of generated carriers G are given by,

$$G(x, \lambda) = \alpha(\lambda)F(\lambda)[1 - R(\lambda)]\exp[-\alpha(\lambda)x] \tag{2.27}$$

where λ is the wavelength of photons, $\alpha(\lambda)$ is the absorption coefficient, $F(\lambda)$ is the number of photons per area per bandwidth, and $R(\lambda)$ is the number of reflected photons per area per bandwidth. First we focus on the carriers in the neutral region in the p-type semiconductor. Under low injection condition, the steady-state continuity equation for minority carriers is,

$$G_n - \frac{n_p - n_{p0}}{\tau_n} + \frac{1}{q}\frac{dJ_n}{dx} = 0 \tag{2.28}$$

where n_p is the electron density in the p-type semiconductor, n_{p0} is that of without light and τ_n is the lifetime of the electrons. The electron current density equation is given by

$$J_n = q\mu_n n_p E + qD_n \frac{dn_p}{dx} \tag{2.29}$$

where μ_n is the mobility of electrons, E is the electric field and D_n is the diffusion constant of electrons. Eq. 2.27, Eq. 2.28, and Eq. 2.29 are combined, and substituting $E = 0$

because there is no electric field at the neutral region, we obtain

$$D_n \frac{d^2 n_p}{dx^2} + \alpha F(1-R)\exp(-\alpha x) - \frac{n_p - n_{p0}}{\tau_n} = 0. \tag{2.30}$$

By solving this with the boundary condition at the surface of the solar cell

$$D_n \frac{dn_p - dn_{p0}}{dx} = S_n(n_p - n_{p0}) \quad (x = 0) \tag{2.31}$$

where S_n is the surface recombination velocity and the boundary condition at the depletion edge

$$n_p - n_{p0} \simeq 0 \quad (x = x_j) \tag{2.32}$$

we can obtain the photocurrent from the neutral region in the p-type semiconductor. The current density from the neutral region in the n-type semiconductor J_p also can be obtained by the same process but using different boundary conditions at the depletion edge ($x = x_j + W$) and at the bottom surface ($x = H$). Next we discuss carriers generated in the depletion region. Carriers generated inside the depletion region are swept out from the depletion region immediately because of the internal electric field. The current density from the carriers generated in the depletion layer J_{dr} is then given by

$$\begin{aligned} J_{dr} &= q\int_{x_j}^{x_j+W} \alpha F(1-R)\exp(-\alpha x)\, dx & (2.33)\\ &= qF(1-R)\exp(-\alpha x_j)[1-\exp(-\alpha W)]. & (2.34) \end{aligned}$$

The total current density per unit bandwidth is,

$$J_{tot}(\lambda) = J_n(\lambda) + J_p(\lambda) + J_{dr}(\lambda) \tag{2.35}$$

and the photocurrent density can be obtained by integration of the bandwidth of the irradiated light. I-V characteristics of a p-n junction under light irradiation is then given by

$$I = AJ_0\left[\exp\left(\frac{qV}{kT}\right) - 1\right] - AJ_L \tag{2.36}$$

where A is the area of the junction, J_0 is the saturation current density of the p-n junction and J_L is the photocurrent density. The current at $V = 0$ is called the short circuit current I_{SC} and voltage at $J = 0$ is called the open circuit voltage V_{OC}. By solving Eq. 2.36 for V at $I = 0$, V_{OC} is given by

$$V_{OC} = \frac{kT}{q}\ln\left[\left(\frac{J_L}{J_0}\right) + 1\right]. \tag{2.37}$$

In the case of Schottky junctions, the photocurrent is also expressed similarly to the case of a p-n junction except for ignoring the photocurrent from the metal and it is given by $J_{tot}(\lambda) = J_s c(\lambda) + J_{dr}(\lambda)$ where J_{SC} is the current density from the semiconductor. If

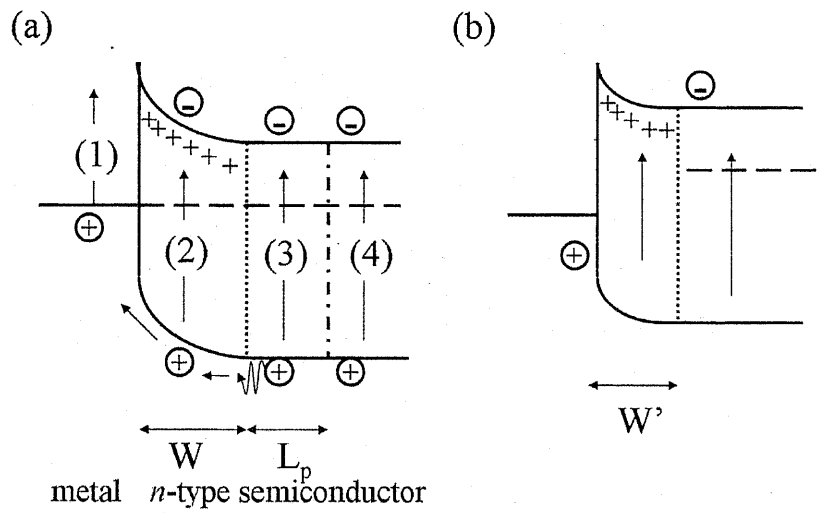

Figure 2.7: Schematic picture of photocarrier injection with the Schottky junction an the n-type semiconductor: (a) just after light irradiation and (b) steady state in the open circuit condition.

we assume I-V characteristics of the Schottky junction is expressed with the thermionic emission model with the ideality factor n, the I-V and V_{OC} are respectively given by

$$I = AA^*T^2 \exp\left(-\frac{q\phi_{bn}}{kT}\right)\left[\exp\left(\frac{qV}{nkT}\right) - 1\right] - AJ_L \tag{2.38}$$

$$V_{OC} = \frac{nkT}{q} \ln\left[\frac{J_L}{A^*T^2 \exp\left(-\frac{q\phi_{bn}}{kT}\right)} + 1\right]. \tag{2.39}$$

2.2.2 Photocarrier injection

We discussed that the photovoltage is given by Eq. 2.37 in the case of a p-n junction and by Eq. 2.39 in the case of a Schottky junction. We discuss more precisely the behavior of generated carriers at the open circuit condition.

Figure 2.7 shows the schematic picture of photocarrier injection. In the case of a Schottky junction with an n-type semiconductor, when light is irradiated, carriers are generated at (1) the metal, (2) the depletion region, (3) within the diffusion length from the depletion edge, and (4) the neutral region. Holes generated in (2) are swept out to the metal because of the internal electric field, and holes generated in (3) reach the depletion edge before recombination and they are also swept out to the metal. The carrier flow by holes in (2) corresponds to J_{dr} and that by holes in (3) corresponds to J_{sc}. Steady state is established when the number of holes injected to the metal in unit time equals the number of holes in the metal which recombine in unit time. The number of holes injected

to the metal is the same as the number of carriers stored in the metal and is given by [14]

$$Q/q = \frac{1}{q}\left[C_{V=V_0}V_{bi} - C_{V=V_{OC}}(V_{bi} - V_{OC})\right] = \sqrt{\frac{2\epsilon_s N_D}{q}}\left(\sqrt{V_{bi}} - \sqrt{V_{bi} - V_{OC}}\right). \quad (2.40)$$

As indicated in the above equation, in order to improve the efficiency of photocarrier injection, it is necessary to increase V_{OC}.

2.2.3 Open circuit voltage decay

The lifetime of carriers is one of the important parameters for photocarrier injection. In fact the lifetime of photocarriers (e.g., τ_n in Eq. 2.28 and Eq. 2.30) is directly related to I_{SC} and V_{OC}. The open circuit voltage decay measurement is one of the methods to obtain the carrier lifetime.

Historically Gossick obtained the carrier lifetime in the neutral region (same as τ_n in Eq. 2.28 and Eq. 2.30) from the measurement of transient behavior of p-n junction by applying a pulsed electric field [15]. Later, Mahan *et al.* modified this method and obtained the lifetime of carriers from the open circuit voltage decay [16]. According to Gossick and Mahan *et al.*, when the light is irradiated (bias voltage V is applied) to for instance, the Schottky junction with an n-type semiconductor, the hole density in the neutral region p_n is given by

$$p_n = p_0 \exp\left(\frac{qV}{kT}\right) = p_{n0} + \Delta p_n \quad (2.41)$$

where p_{n0} is the steady state carrier density of holes and Δp_n is the excess carrier density. Solving this equation for Δp_n gives

$$\Delta p_n = p_{n0}\left[\exp\left(\frac{qV}{kT}\right) - 1\right]. \quad (2.42)$$

If the light is turned off at time $t = 0$, excess carriers recombine with the lifetime of τ_p and this is expressed with

$$\Delta p_n(t) = \Delta p_n\,|_{(t=0)} \exp\left(-\frac{t}{\tau_p}\right). \quad (2.43)$$

From Eq. 2.42 and Eq. 2.43, we obtain the open circuit voltage decay as

$$V(t) = V(0) - \frac{kTt}{q\tau_p} \qquad V(t) \gg \frac{kT}{q} \quad (2.44)$$

$$V(t) = \frac{kT}{q}\left[\exp\left(\frac{qV(0)}{kT}\right) - 1\right]\exp\left(-\frac{t}{\tau_p}\right) \qquad V(t) \ll \frac{kT}{q}. \quad (2.45)$$

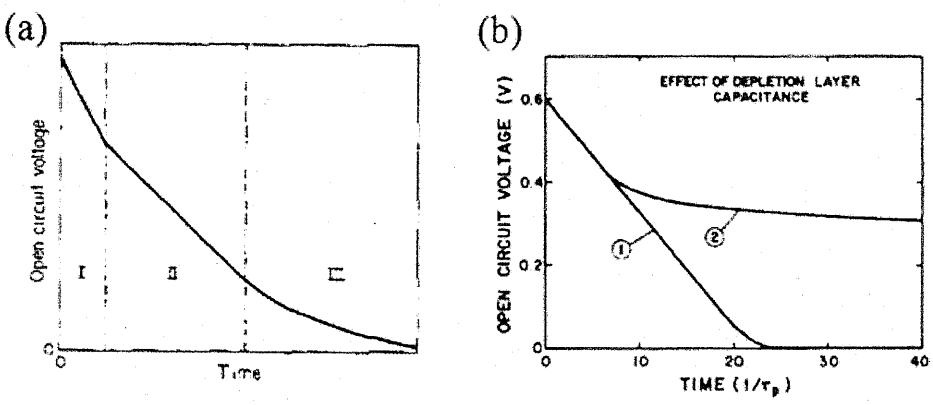

Figure 2.8: (a) The theoretical open circuit voltage decay [16]. (b) The open circuit voltage decay when the junction capacitance is nonnegligible [19].

According to Wilson [17] and Bassett [18], the lifetime at the condition of $V(t) \gg \frac{kT}{q}$ is given by

$$\tau_p = \frac{2kT}{q\frac{dV}{dt}} \qquad p_n \gg N_D \tag{2.46}$$

$$\tau_p = \frac{kT}{q\frac{dV}{dt}} \qquad p_n \ll N_D \tag{2.47}$$

$$\tag{2.48}$$

and the theoretical open circuit voltage decay is shown in Fig. 2.8 (a).

In the above theory, only the contribution of carriers generated in the neutral region ((3) and (4) in Fig. 2.7) is taken into consideration. Mahan *et al*, considered the effect of carriers stored in the depletion layer [19]. When the depletion layer capacitance is large and carriers stored in the depletion region is nonnegligible, the open circuit voltage decay differs from the previous theory (Fig. 2.8 (b)). In cases where $V_{OC} \ll V_{bi}$ holds, and assume the lifetime of stored charges, τ_{SC}, decrease exponentially, Eq. 2.40 is modified to

$$Q_0 \exp\left(-\frac{t}{\tau_{SC}}\right) \simeq \sqrt{\frac{2\epsilon_s N_D}{q}}\left[\sqrt{V_{bi}} - \sqrt{V_{bi}}\left(1 - \frac{V(t)}{2V_{bi}}\right)\right] \tag{2.49}$$

and the open circuit voltage decay is simply expressed as

$$V(t) \propto \exp\left(-\frac{t}{\tau_{SC}}\right) + \text{Const.} \tag{2.50}$$

Now the relation between lifetimes of photocarriers and the open circuit voltage decay is summarized in Tab. 2.1. When the depletion region is small, injected carriers to the metal are mainly carriers generated in the neutral region in the n-type semiconductor, so the minority carrier lifetime in the semiconductor affects the number of injected carriers.

depletion capacitance	characteristic lifetime for carrier injection	open circuit voltage decay
small	τ_p	linear
large	τ_{sc}	exponential

Table 2.1: Table of the relation between carrier lifetimes and open circuit voltage decay.

On the other hand, when the depletion region is large and most of the injected carriers are generated in the depletion region, the depletion capacitance become nonnegligible and injected carriers are equal to the stored charge in the depletion capacitance. So the lifetime of stored charges represent the number of injected carriers. In the former case, the open circuit voltage decreases linearly and in the latter case, the open circuit voltage decreases exponentially.

Chapter 3

Review of the electrical properties of Au/Nb:$SrTiO_3$ junctions

In this chapter we review the electrical properties of Au/Nb : $SrTiO_3$ junctions which have been intensively studied as a model case for junctions using $SrTiO_3$ and other oxides. For the help of understanding, we also review the physical properties of $SrTiO_3$.

3.1 Brief review of the physical properties of $SrTiO_3$

$SrTiO_3$ has a cubic perovskite structure with a lattice constant of 3.905 Å at room temperature (Fig. 3.1). It shows a phase transition to a tetragonal structure around 110 K [20]. $SrTiO_3$ itself is a band insulator with the band gap of 3.2 eV [21], but by substituting Ti by Nb, Sr by La or by reduction, it shows an insulator to metal transition at a carrier concentration of 10^{18} cm^{-3} and becomes an n-type semiconductor [22, 23, 24]. Because of the large dielectric permittivity [25], the electron mobility can exceed 10^4 cm^2/Vs at low temperature [23]. As the result of large mobility, large photoconductivity is observed at low temperatures [26, 27, 28]. Photocarrier doped $SrTiO_3$ also shows n-type conduction [26]. This large permittivity and the photoconductivity are advantageous for photocarrier injection.

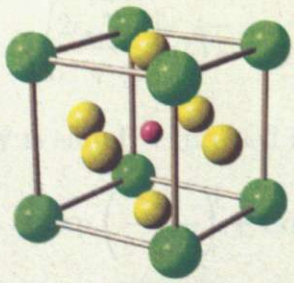

Figure 3.1: Unit cell of $SrTiO_3$. O^{2-} ions are octahedrally-coordinated around a Ti^{4+} ion. Sr^{2+} ions are coordinated at the corners of the unit cell.

3.2 Electrical properties of Au/Nb:$SrTiO_3$ junctions

First we review the previous study about the band alignment between Au and Nb:$SrTiO_3$. The work function of Au and the electron affinity of $SrTiO_3$ is 5.1 eV and 3.9 eV, respectively [29], so it follows that from the Schottky-Mott model, the Schottky barrier with the barrier height of 1.2 eV should be formed at the Au and semiconducting $SrTiO_3$ contacts. Neville *et al.* measured the barrier height of contacts of Au and reduced $SrTiO_3$ prepared by different surface treatments and they obtained almost the same values as expected from the Schottky-Mott model independently. According to Kurtin *et al.*, the S parameter, which represents the ionicity of crystal, is more than 1 [11] and this automatically means the metal and $SrTiO_3$ contacts are described by the Schottky-Mott relation. However, recently some studies are suggesting S parameter of $SrTiO_3$ is much less than 1 [29]. If the band alignment is described by the Bardeen model, the number of surface states must be important for the formation of the barrier. Number of the surface states in the gap of $SrTiO_3$ was estimated to be 10^{15} cm^{-2} by Morin *et al.* [31], but Powell *et al.* measured the number of the surface states by photoemission and they conclude the number is less than 10^{12} cm^{-2} [32] and the number is small. In conclusion, mechanisms to describe the barrier height between Au and $SrTiO_3$ are still controversial.

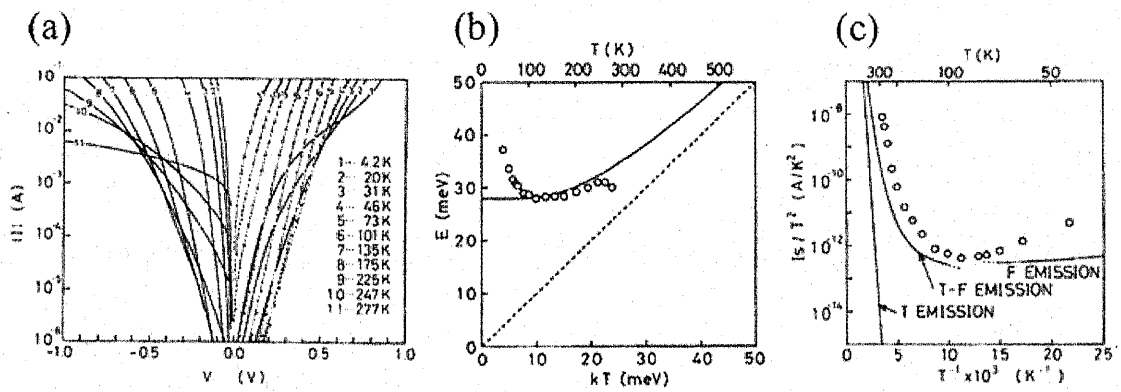

Figure 3.2: Temperature dependent electrical properties of Au/Nb : $SrTiO_3$ junctions: (a) I-V characteristics (b) parameter E_0 of Eq. 2.22 and (c) the saturation current as a function of temperature.

Next we review the junction transport properties across Au/Nb : $SrTiO_3$ junctions. Hasegawa *et al.* investigated the temperature dependence of the I-V characteristics of Au/Nb:$SrTiO_3$ junctions (Fig. 3.2 (a)) [33] and they revealed that the current transport processes are described by the thermionic emission and the thermionic-field emission model at temperatures above 101 K (Fig. 3.2 (b), (c)). At temperature lower than 100

K, thermionic-field emission and field emission can not explain the behavior and indicates the existence of current process other than these current transport processes. One of the possibilities of this additional current at lower temperatures is considered to be due to the temperature and the electric field dependence of the dielectric permittivity of $SrTiO_3$.

According to Barrett's formula [35], the temperature dependent permittivity of $SrTiO_3$ is expressed as

$$\epsilon_r(T) = \frac{1635}{\coth\left(\frac{44.1}{T}\right) - 0.937} \tag{3.1}$$

and the electric field dependence of permittivity is given by $\epsilon_r(E) = \frac{b}{\sqrt{a+E^2}}$ where a and b are fitting parameters [36]. Yamamoto *et al.* [37] combined these formulae and derived the following,

$$\epsilon_r(T,\ E) = \frac{b(T)}{\sqrt{a(T) + E^2}} \tag{3.2}$$

with the relation $a(T) = [b(T)/\epsilon_r(T)]^2$ and $b(T) = 1.37 \times 10^9 + 4.29 \times 10^7\ T$ V/m. From these formulae, the depletion layer width and the potential variation is given by

$$W = \frac{b(T)\epsilon_0}{qN_D}\cosh^{-1}\left[1 + \frac{qN_D}{\sqrt{a(T)}b(T)\epsilon_0}(-V + \phi_{bn})\right] \tag{3.3}$$

and

$$V_{bi}(x) = \frac{\sqrt{a}b(T)\epsilon_0}{qN_D}\cosh\left\{\left[\frac{qN_D}{b(T)\epsilon_0}(W - x)\right] - 1\right\} + V. \tag{3.4}$$

where ϵ_0,are vacuum permittivity. The permittivity of $SrTiO_3$ increases with decreasing the temperature, however, because of the large electric field near the interface, the permittivity near the interface is extremely reduced at low temperature and as a result, the band bending become sharp (Fig. 3.4). This sharpening of the band bending increases the tunneling probability and results in extra current flow at low temperatures.

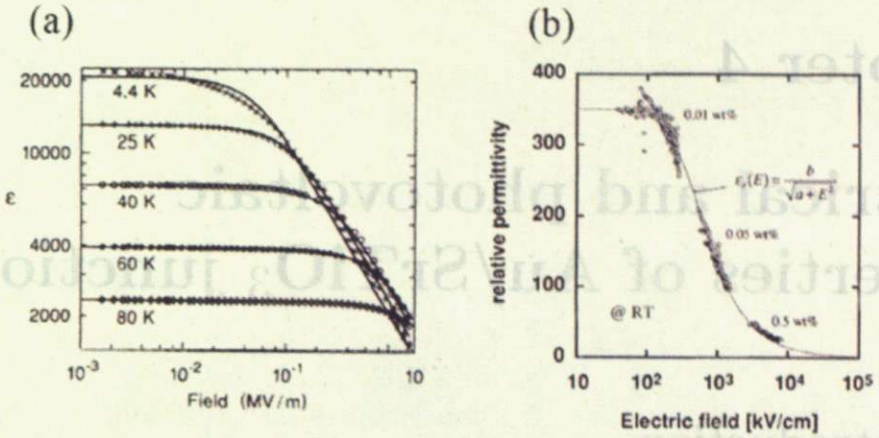

Figure 3.3: (a) Temperature dependence [36], and (b) the electric field dependence of the permittivity of $SrTiO_3$ [38].

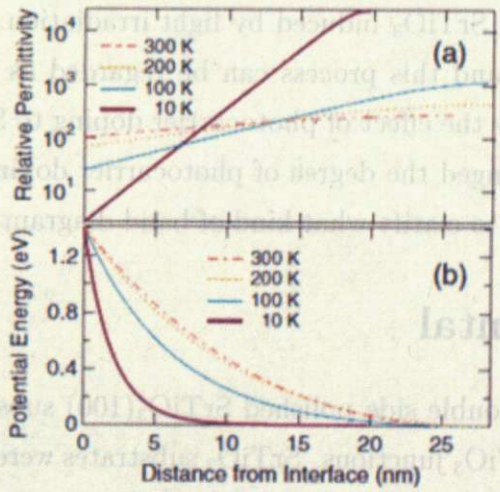

Figure 3.4: The simulated permittivity and the potential energy variation with distance from the interface. The Schottky barrier height and the carrier density of $SrTiO_3$ are fixed to 1.41 eV and 5×10^{19} cm^{-3} in this calculation [39].

Chapter 4

Electrical and photovoltaic properties of Au/$SrTiO_3$ junctions

4.1 Introduction

Pioneering experiments on photocarrier injection in oxides by Katsu *et al.* were studied in a$La_{1-x}Sr_xMnO_3$/ $SrTiO_3$ structure [8]. However, in this study it is not obvious what kind of band alignment is realized between $La_{1-x}Sr_xMnO_3$ and $SrTiO_3$because $SrTiO_3$is an insulator. When a metal and an insulator is attached, band bending should not occur because of the absence of fixed charges. In contrast, if only photogenerated holes are selectively injected in $La_{1-x}Sr_xMnO_3$and as a result physical properties are changed, some barrier, for example the Schottky barrier, should block electrons generated in $SrTiO_3$ to be injected in $La_{1-x}Sr_xMnO_3$. This indicates the possibility of band bending and formation of barrier for electrons in $SrTiO_3$ induced by light irradiation. $SrTiO_3$ is known to show large photoconductivity and this process can be regarded as self photo-doping. In this chapter, in order to study the effect of photocarrier doping to $SrTiO_3$ on the photocarrier injection process, we changed the degree of photocarrier doping at the interface between Au and $SrTiO_3$. We aim to clarify what kind of band diagram is realized at the interface.

4.2 Experimental

We used 0.5 mm thick double side polished $SrTiO_3$(100) substrates (Furuuchi Chemical Co.) to fabricate Au/$SrTiO_3$ junctions. $SrTiO_3$ substrates were annealed in UHV chamber at 800 °C ,oxygen patial pressure of 2×10^{-5} Torr, for 30 minutes to clean the surface and 30 nm Au was evaporated *in-situ* by e-beam evaporation . Al was wire-bonded as the back contact. The areas of the junctions were about 0.004 cm^2. The experimental set up is shown in Fig. 4.1. For low temperature measurements, samples were studied in a liquid Helium cryostat Physical Property Measurement System (PPMS, Quantum Design Co.). We employed a Xe lamp as the light source (LAX 102, Asahi Spectra Co.) and the

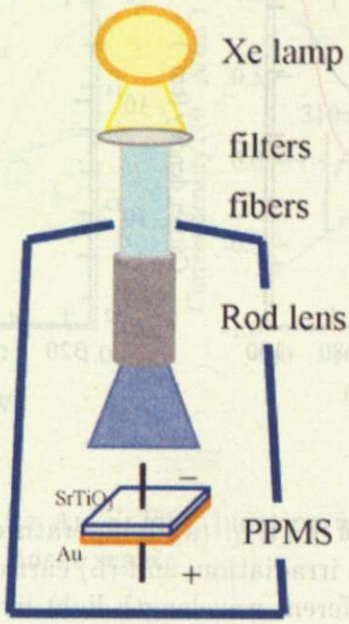

Figure 4.1: Experimental setup and measurement geometry. Light was irradiated from the back of the Au/$SrTiO_3$ junctions.

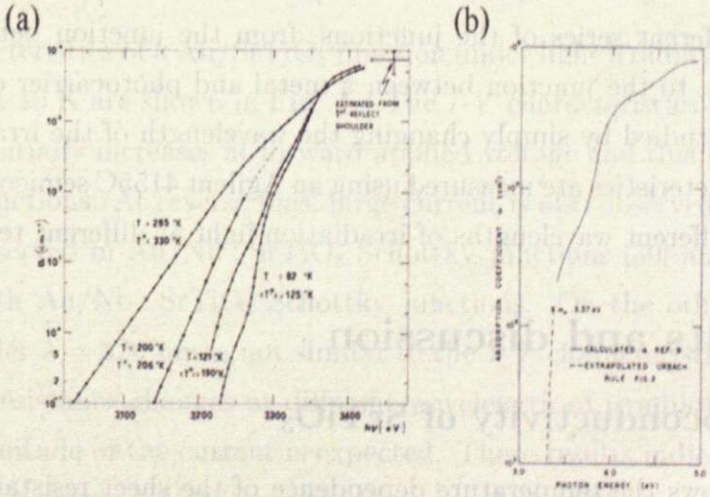

Figure 4.2: Absorption coefficient of $SrTiO_3$: (a) near band edge [41] and (b) at higher photon energy [40].

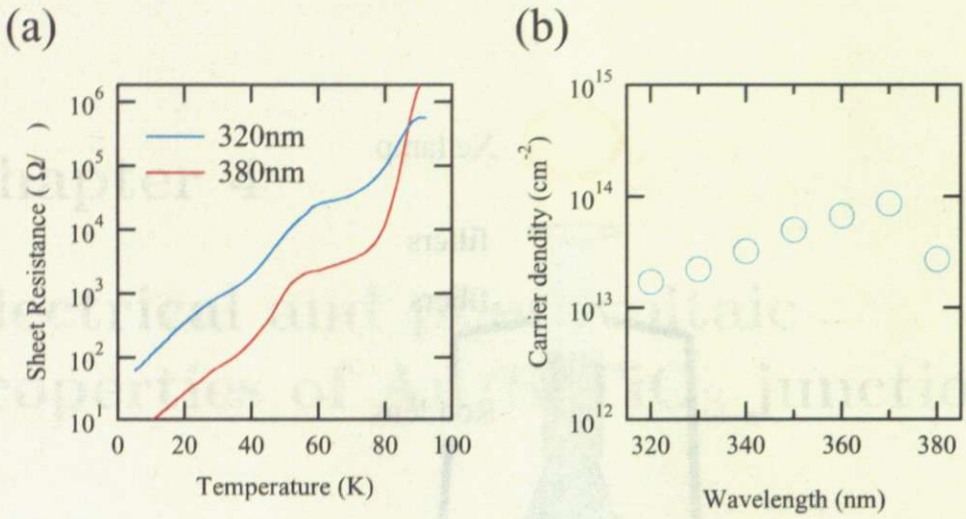

Figure 4.3: Photoconductivity of $SrTiO_3$: (a) Temperature dependence of sheet resistance under different wavelength light irradiation, and (b) carrier density determined from Hall measurement at 10 K under different wavelength light irradiation.

light was band-pass filtered with the bandwidth of 10 nm. The light was irradiated from the back of the $SrTiO_3$ substrates. Figure 4.2 shows the absorption coefficient of $SrTiO_3$ [40, 41]. These experimental results show that the optical penetration length (inverse of the absorption coefficient) of $SrTiO_3$ becomes longer with increasing the wavelength of the irradiated light. This indicates that when light of shorter wavelength is irradiated to the junction from the back, photocarriers are generated only at the surface of $SrTiO_3$, and when the wavelength is larger, photocarriers are generated an extended larger region. Therefore the different series of the junctions, from the junction between a metal and insulating $SrTiO_3$, to the junction between a metal and photocarrier doped $SrTiO_3$, can be achieved and studied by simply changing the wavelength of the irradiated light.

The *I-V* characteristics are measured using an Agilent 4155C semiconductor parameter analyzer under different wavelengths of irradiation light at different temperatures.

4.3 Results and discussion

4.3.1 Photoconductivity of $SrTiO_3$

Figure 4.3 (a) shows the temperature dependence of the sheet resistance under different wavelength. The light intensity is fixed to about 0.5 W/cm^2. The difference of the resistance in the case of 320 nm irradiation and 380 nm irradiation is mainly because of the difference in the spatial distribution of photocarriers. The temperature dependence of the sheet resistance was similar for both cases. Figure 4.3 (b) shows the carrier density

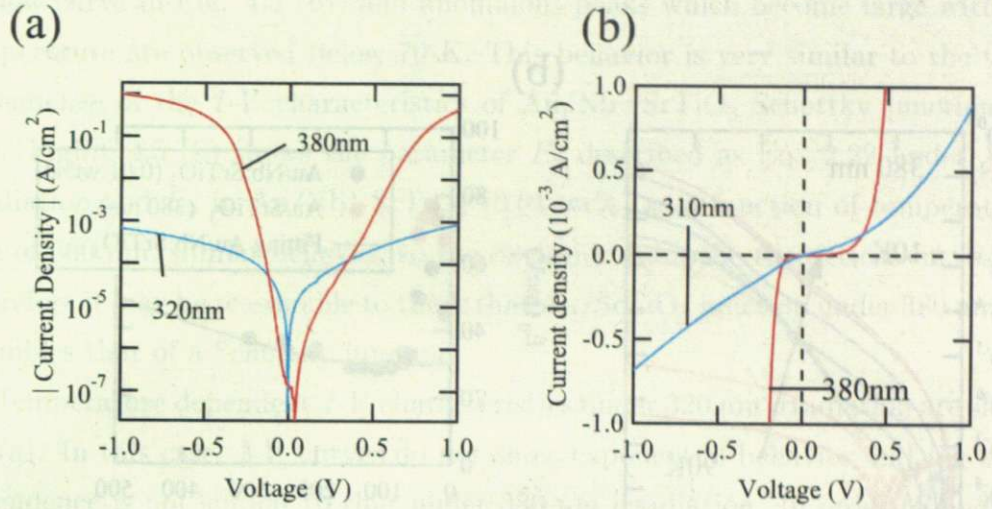

Figure 4.4: *I-V* characteristics for Au/$SrTiO_3$ junction under 320 nm and 380 nm irradiation at 10 K: (a) log scale (b) linear scale.

of $SrTiO_3$ under different wavelength of light irradiation at 10 K. The carrier density slightly increases at longer wavelength and decreases at 380nm irradiation. The slight increase corresponds to the slight difference of light intensity, and the decrease at 380 nm irradiation is attributed to the longer optical penetration length competed to the thickness of the $SrTiO_3$ substrate. The sheet carrier density measured by Hall measurement was then almost independent on the wavelength.

4.3.2 Current transport processes

Typical *I-V* characteristics of a Au/$SrTiO_3$ junction under light irradiation by $\lambda = 320$ nm and $\lambda = 380$ nm at 10 K are shown in Fig. 4.4.The *I-V* characteristics under $\lambda = 380$ nm irradiation exponentially increases at forward applied voltage and this behavior is similar to the Schottky junctions. At reverse bias, large current is also observed, but this polarity reversal is also observed in Au/Nb : $SrTiO_3$ Schottky junctions [39] and this behavior is also consistent with Au/Nb : $SrTiO_3$ Schottky junctions. On the other hand, The *I-V* characteristics under $\lambda = 320$ nm is not similar to the *I-V* characteristics of $\lambda = 380$ nm. If only the series resistance changes at different wavelength of irradiation light, only the change in the magnitude of the current is expected. These results indicates the transport process is different between $\lambda = 320$ nm irradiation and $\lambda = 380$ nm irradiation.

Figure 4.5 (a) shows the temperature dependence of the *I-V* characteristics under $\lambda = 380$ nm irradiation. The *I-V* curves were measured every 10 K from 10 K to 90 K. Because of poor photoconductivity at higher temperatures, the effect of series resistance cannot be neglected. However, exponential behavior of the *I-V* curves are observed at 70K

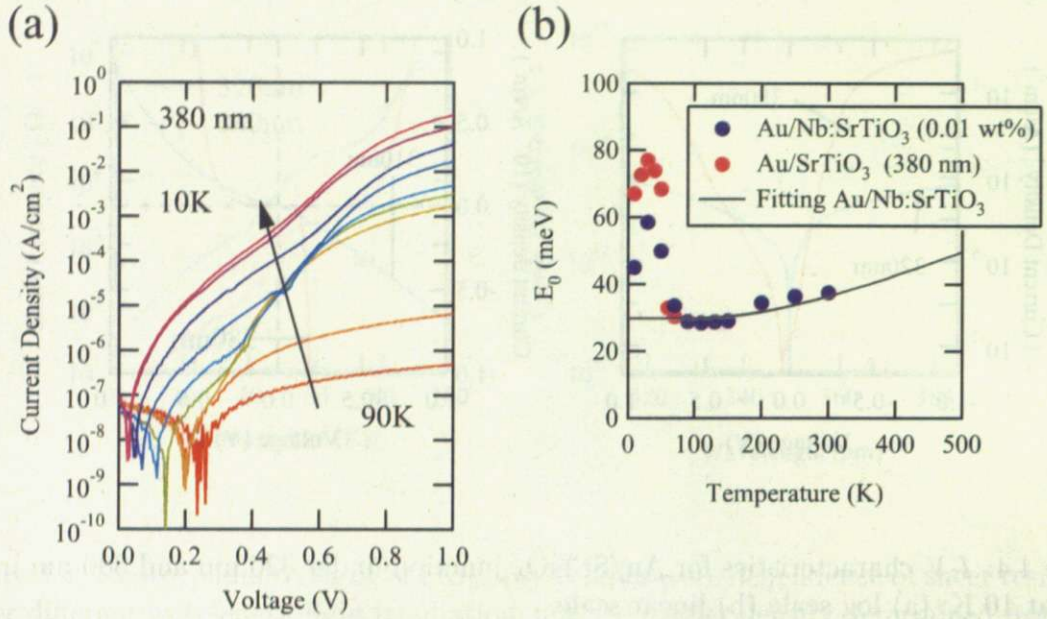

Figure 4.5: (a) Temperature dependence of the *I-V* characteristics of Au/$SrTiO_3$ under 380 nm irradiation. (b) Thermionic-field emission parameter $E0$ as a function of temperature.

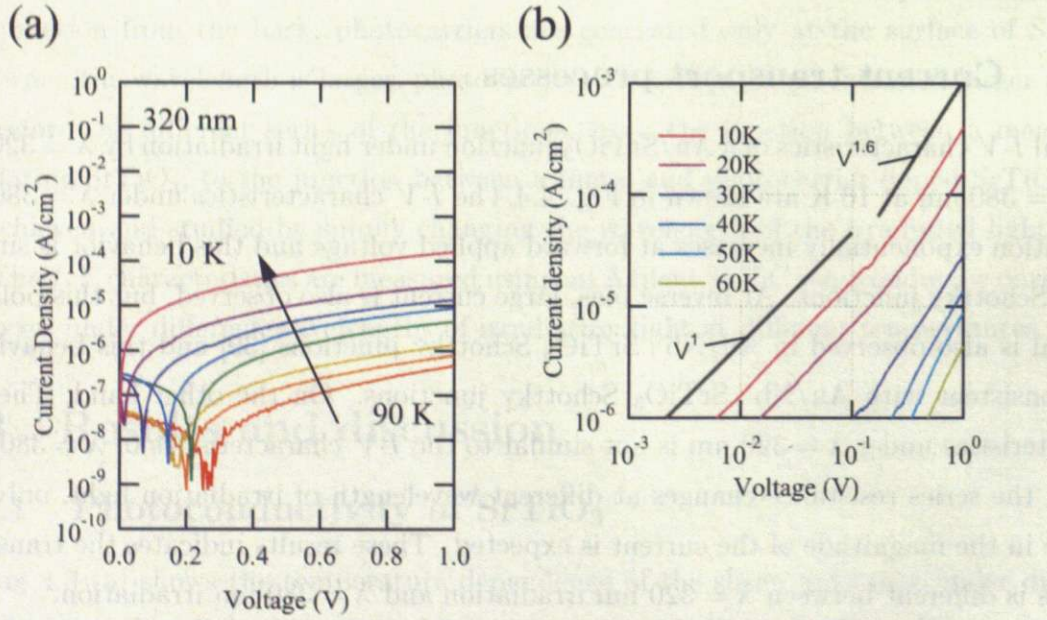

Figure 4.6: Temperature dependence of the *I-V* characteristics of Au/$SrTiO_3$ under 380 nm irradiation: (a) semi-logarithmic scale (b) logarithmic scale.

(yellow curve in Fig. 4.5 (b)) and anomalous peaks which become large with decreasing temperature are observed below 70 K. This behavior is very similar to the temperature dependence of the I-V characteristics of Au/Nb : $SrTiO_3$ Schottky junctions (Fig. 3.2 (a)). Figure 4.5 (b) shows the parameter E_0 described as Eq. 2.22 under $\lambda = 380$ nm irradiation and E_0 in Au/Nb : $SrTiO_3$ (0.01 wt%) as a function of temperature. In the case of 380 nm, similar behavior to the deviation from the theoretical curve is observed. Therefore it may be reasonable to think that Au/$SrTiO_3$ junction under 380 nm irradiation resembles that of a Schottky junction.

Temperature dependent I-V characteristics under 320 nm irradiation are shown in Fig. 4.6 (a). In this case, I-V curves do not show exponential behavior and the temperature dependence is not similar to that under 380 nm irradiation. In order to understand the current transport mechanism, the logarithmic plot of the I-V curves are shown in Fig. 4.6 (b). The current is proportional to V at lower applied voltage, which could indicate ohmic conduction. However, clear kinks are observed in these I-V curves at around 0.1 V and the relation $J \propto V^{1.6}$ is observed at large applied voltages. These experimental results indicate that these current processes are not simple ohmic conduction.

Considering various models of conduction, in the case of unipolar conduction in insulators, it is known that current transport is proportional to the square of the applied bias voltage because of the absence of compensating charges [42]. Suppose an insulator with ohmic contact electrodes in the dark, at low applied voltage, conduction of thermally generated carriers which follow Ohm's law is the dominant process and this current is expressed as $J_{ohm} = qn\mu V/d$, where n is the carrier density of the insulator, d is the length of the insulator and μ is mobility of carriers. At large apply voltage, the conduction of carriers injected from the electrode via space charge limited (SCL) conduction becomes the dominant conduction process and this process is described as $J_{SCL} = 9/8\epsilon\mu V^2/d^3$ where ϵ is the permittivity of the insulator.

In this case, carriers are generated only near the surface of $SrTiO_3$ (absorption coefficient of 320 nm is about 30 nm^{-1}), thus the conduction of these carriers are thought to be SCL conduction. At low temperatures, thermally generated carriers are negligibly small, and the voltage at which the conduction mechanism switches may be small. One possible origin of the kinks of the I-V curves under 320 nm is this switching of conduction from ohmic to SCL conduction. However, no temperature dependence is observed in the shift of kinks. Moreover, the current caused by thermally generated carriers should be much smaller than the observed current at low voltage. These results are inconsistent with this model, so the current transport process is still unclear. However, the current process under 320 nm irradiation seems bulk limited rather than that of a Schottky junction.

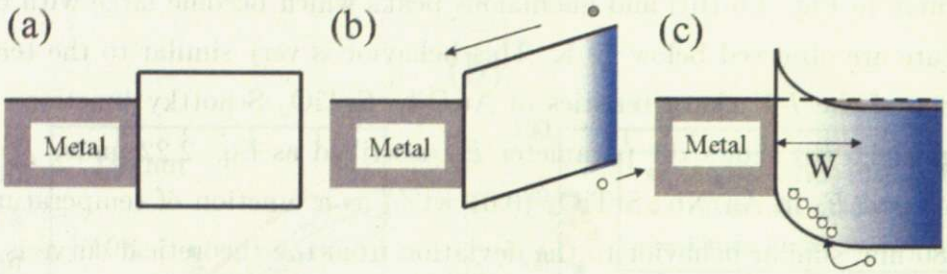

Figure 4.7: Band diagrams of the Au/$SrTiO_3$ junction: (a) in the dark (b) under 320 nm irradiation and (c) under 380 nm irradiation.

4.3.3 Estimation of Au/$SrTiO_3$ junctions under light irradiation

We summaries the results of *I-V* characteristics as:

1. The *I-V* characteristics under 380 nm irradiation is similar to Au/Nb : $SrTiO_3$ Schottky junctions.

2. The *I-V* characteristics under 320 nm irradiation is bulk limited conduction such as ohmic and SCL conduction.

3. 320 nm irradiation is more conducting than 380 nm irradiation at low applied voltage.

Now we estimate the band diagrams at Au/$SrTiO_3$ interface. First, under 380 nm irradiation, it is reasonable to think that a Schottky junction is formed. On the other hand, under 320 nm irradiation, the results 2 and 3 indicate that band bending is not formed and the conduction is bulk limited. This is because, if the Schottky barrier is formed, the current at low applied voltage should be limited by the Schottky barrier and the current under 320 nm irradiation never exceeds the current under 380 nm irradiation.

At the interface beteen a metal and a pure insulator, because of the absence of fixed charges such as dopants, there should not be a space charge region, and band bending should not occur even if there is a difference between the work function of the metal and the electron affinity of the insulator, even if there are surface states. In the case of insulating $SrTiO_3$, oxygen deficiently is relatively easily introduced and this can act as the donor, but resistances of our samples are more than 1 GΩ, so we can ignore the effect of the oxygen deficiency and other possible intrinsic origins of fixed charge.

One possible origin to form the Schottky barrier and to induce band bending under 380 nm irradiation is the trapped holes close to the interface of Au and $SrTiO_3$. In the case of 380 nm irradiation, optical penetration length is longer than the thickness of the $SrTiO_3$ substrate and carriers are also generated close to the interface. The mobility of

holes in $SrTiO_3$ is much smaller than that of electron [43], and holes can be easily trapped or localized in $SrTiO_3$. Actuallty, it is known that holes are localized at O_2^{3-} centers when light is irradiated [44] and these can act as positive quasi-fixed charge. Those localized holes near the junction can act as the fixed charges and as a result induce band bending. In contrast, under 320 nm irradiation, almost all photons are absorbed only near the surface of $SrTiO_3$, so carrier are not generated at the junction of Au and $SrTiO_3$, thus band bending can not occur.

4.4 Conclusions

In this study we have investigated the effect of the photocarrier doping to the $SrTiO_3$ by photocarrier injection and we confirmed the possibility of band bending under light irradiation. This implies that band bending induced by photocarrier doping may stongly affect the properties of photocarrier injection.

Chapter 5

Electrical and photovoltaic properties of Au/Nb:$SrTiO_3$ junctions

5.1 Introduction

As shown in Chapter 1, in order to control the doping level in the photocarrier injection technique, precise control of the open circuit voltage (V_{OC}) is needed because the number of the injected carriers and V_{OC} is directly related. Moreover, the open circuit voltage reflects the junction properties such as dark current, so it is necessary to understand the electrical properties of the junction comprehensively. We also mentioned that Au/$SrTiO_3$ junctions are the most simple model for these studies. In Chapter 3, we reviewed the electrical properties of Au/Nb : $SrTiO_3$ and we know an additional current process is observed at low temperatures, possibly originating from the temperature and the electric field dependence of the permittivity of $SrTiO_3$. In this chapter, we focus on the effect of the electric field dependence of $SrTiO_3$ in the photocarrier injection process, and we will discuss the efficiency of the photocarrier injection method. We adopted Au/Nb : $SrTiO_3$ as the simple case of the junction and we measured the photovoltaic properties such as V_{OC}, the short circuit current (I_{SC}) as well as the electrical properties in the dark. We also measured the V_{OC} transient decay to obtain the lifetime of photocarriers to determine the properties of the photocarriers after injection to the metal.

5.2 Experimental

We prepared Au/Nb : $SrTiO_3$ (0.01wt%) junction for the measurements. About 200 Å Au was evaporated on to Nb : $SrTiO_3$(100) substrates (Furuuchi Chem. Co) after cleaning the surface in air. Typical size of the junctions is 0.005 cm^2. All measurement were carried out in the PPMS. The I-V characteristics and the C-V characteristics are measured with a Keithley 2401 sourcemeter and an Agilent 4284A LCR meter, respectively, in the dark.

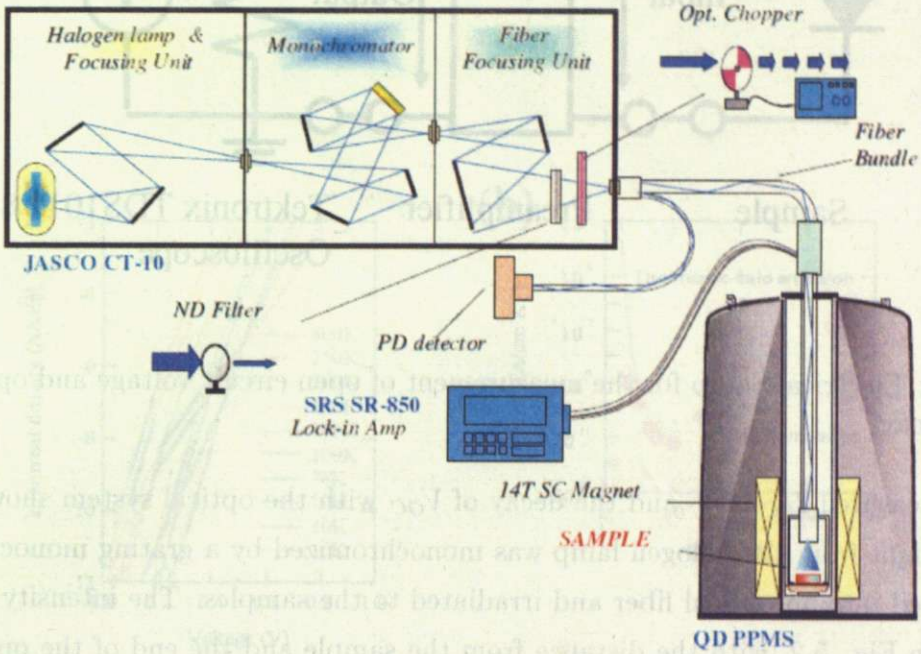

Figure 5.1: The optical system for the measurement of photovoltaic properties [45].

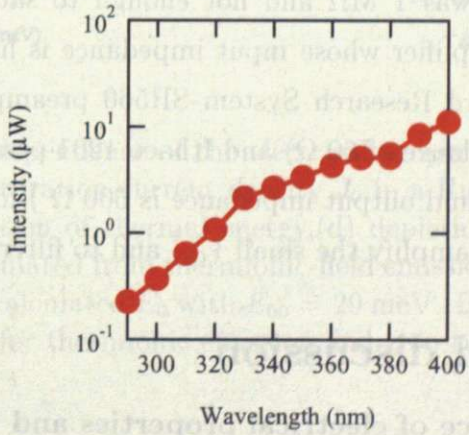

Figure 5.2: Wavelength dependence of light intensity.

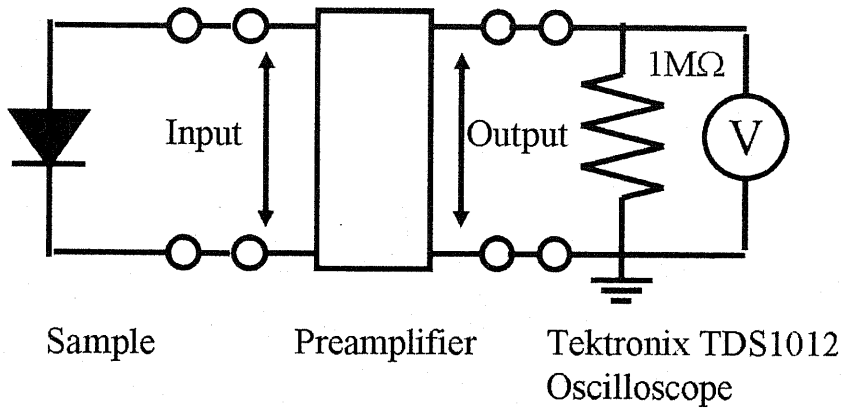

Figure 5.3: Electrical Setup for the measurement of open circuit voltage and open circuit voltage decay.

We also measured I_{SC}, V_{OC} and the decay of V_{OC} with the optical system shown in Fig. 5.1 [45]. Light from the halogen lamp was monochromized by a grating monochromator, then focused into an optical fiber and irradiated to the samples. The intensity spectrum is shown in Fig. 5.2, with the distance from the sample and the end of the optical fiber fixed to 3 mm. For the measurement of I_{SC}, we also used the Keithley 2401 sourcemeter.

Figure. 5.3 shows the circuit diagram of the electrical setup of the measurement for the open circuit voltages and the decay of V_{OC}. In order to measure the correct V_{OC} and V_{OC} decay, the input impedance the voltmeter should be as high as possible. For the measurement of V_{OC} decay, the maximum lifetime we can correctly measure from the decay of $\tau_{V_{OC}}$ is limited by the time constant $\tau_{RC} = RC$ where C is the junction capacitance and R the input impedance. We used a Tektronix TDS1012 oscilloscope for the measurement, but the input impedance was 1 MΩ and not enough to satisfy the requirement. We connected a voltage preamplifier whose input impedance is high and output impedance is low. We used a Stanford Research System SR560 preamplifier (input impedance is 100 MΩ with output impedance of 60 Ω) and Ithaco 1201 preamplifier (input impedance is more than 100 MΩ and and output impedance is 600 Ω) for the measurement. These preamplifiers were used to amplify the small V_{OC} and to filter out the noise.

5.3 Results and discussion

Temperature dependence of electrical properties and photovoltaic properties

Figure 5.4 (a) shows the temperature dependence of the I-V characteristics in Au/Nb:$SrTiO_3$. As shown in Chapter 3, anomalous peaks are observed at low temperature. Saturation current J_0 is estimated from the linear fitting of the logarithm of the current density which

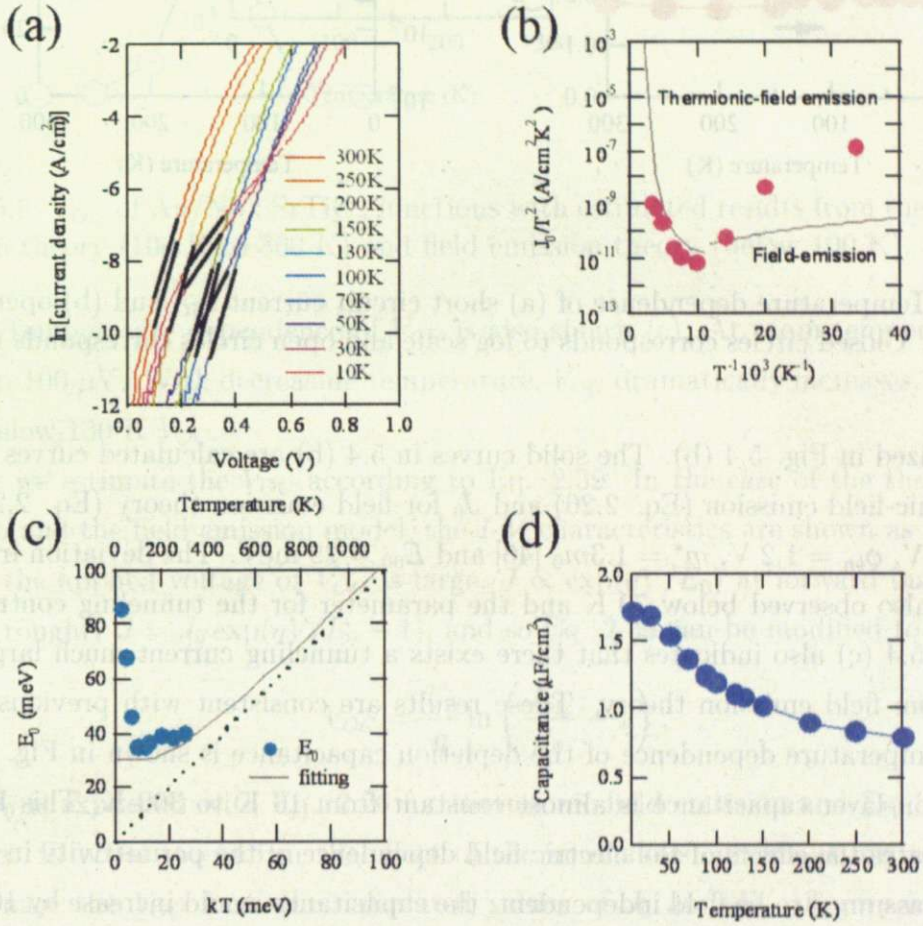

Figure 5.4: Temperature dependence of the electrical properties of Au/Nb : $SrTiO_3$: (a) *I-V* characteristics, (b) saturation current density J_0 in a Richardson plot, (c) tunneling contribution E_0 as a function of thermal energy,(d) depletion capacitance at zero bias. Solid curves in (b) are calculated from thermionic-field emission and field emission models and solid curves in (c) are calculated E_0 with $E_{00} = 29$ meV. Broken line in (c) is $E_0 = kT$, which represents the case for thermionic emission and zero tunneling contribution.

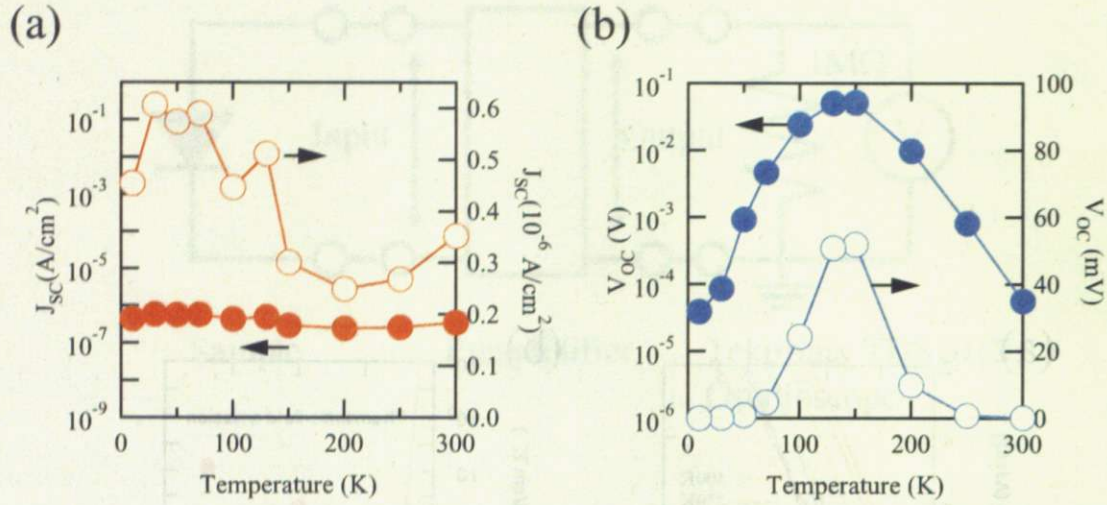

Figure 5.5: Temperature dependence of (a) short circuit current I_{SC} and (b) open circuit voltage V_{OC}. Closed circles corresponds to log scale and open circles corresponds to linear scale.

are summarized in Fig. 5.4 (b). The solid curves in 5.4 (b) are calculated curves from J_0 for thermionic-field emission (Eq. 2.26) and J_0 for field emission theory (Eq. 2.25) with $V_n = -6$ meV, $\phi_{bn} = 1.2$ V, $m^* = 1.3m_0$ [46] and $E_{00} = 29$ meV. The deviation from field emission is also observed below 70 K and the parameter for the tunneling contribution, E_0, in Fig. 5.4 (c) also indicates that there exists a tunneling current much larger than expected from field emission theory. These results are consistent with previous studies [33]. The temperature dependence of the depletion capacitance is shown in Fig. 5.4 (d). The depletion layer capacitance is almost constant from 10 K to 300 K. This behavior clearly indicates the effects of the electric field dependence of the permittivity in $SrTiO_3$, for if ϵ were assumed to be field independent, the capacitance would increase by 100 times from 300 K to 10 K.

Next we focus on the photovoltaic properties of Au/Nb : $SrTiO_3$ junctions. Figure 5.5 shows the temperature dependence of I_{SC} under 340 nm irradiation divided by the junction area (J_{SC}). J_{SC} is almost constant at higher temperature but gradually increases with decreasing temperature. According to the theory of solar cells, I_{SC} is the flow of carriers generated in the depletion layer and within the distance of the diffusion length of the carriers from the depletion edge. In the case of $SrTiO_3$, the lifetime of carriers from photoluminescence measurement is about 1 ms at 10 K and decreases with increasing temperature [47], and the drift mobility of the holes are measured to be of the order of 10 cm^2/Vs at 4 K [43]. On the other hand, it is known that photogenerated holes are localized as O_2^{3-} center [44] so it cannot be thought that holes are so mobile in the neutral

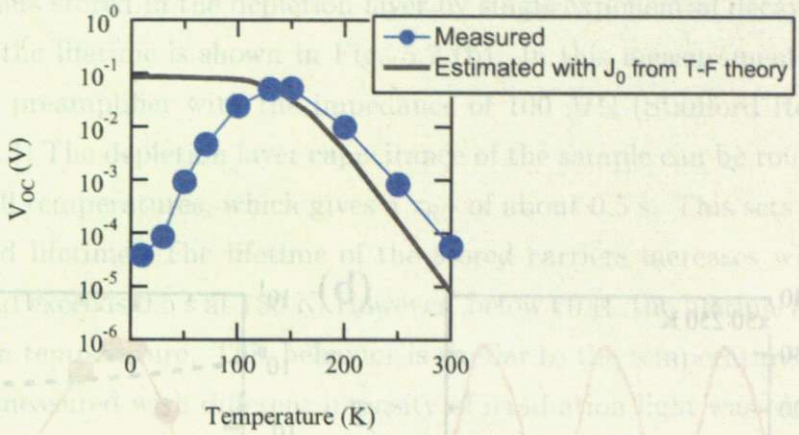

Figure 5.6: V_{OC} of Au/Nb : $SrTiO_3$ junctions with estimated results from thermionic-field emission theory (100 K to 300 K) and field emission theory (below 100 K).

region. Temperature dependence of V_{OC} is also shown (c). At room temperature V_{OC} is less than 100 μV. With decreasing temperature, V_{OC} dramatically increases, but decrease again below 130 K V_{OC}.

Now we estimate the V_{OC} according to Eq. 2.39. In the case of the thermionic-field emission and the field emission model, the I-V characteristics are shown as Eq. 2.21. As long as the applied voltage or V_{OC} is large, $J \propto \exp(qV/E_0)$ at forward bias, so we can assume roughly $J = J_0 \exp(qV/E_0 - 1)$, and so Eq. 2.39 can be modified to

$$V_{OC} = \frac{E_0}{q} \ln\left(\frac{J_{SC}}{J_0} + 1\right), \tag{5.1}$$

where J_0 is expressed with Eq. 2.26 for thermionic-field emission and Eq. 2.25 for field emission. In order to confirm the effect of the anomalous current at low temperatures, we estimate the V_{OC} from the calculated values of J_0 and E_0. Figure 5.6 shows the estimated value of V_{OC} and the measured V_{OC} as a function of temperature. If we assume thermionic-field emission and field emission theory, we can confirm the dramatic increase of V_{OC} at higher temperature as well as the measured V_{OC}. In contrast, the estimated value of V_{OC} saturates with decreasing temperature. This indicates that the anomalous current at low temperature results in the decrease of V_{OC} and the consequent reduction of the efficiency of the photocarrier injection.

Open circuit voltage decay

We also estimated the lifetime from the measurement of the open circuit voltage decay. Typical decays of V_{OC} under 340 nm irradiation are shown in Fig. 5.7 (a). As shown in the figures, V_{OC} does not seem to decay linearly. This implies the carriers stored in the depletion region is larger than the carriers stored in the neutral region. We extracted the

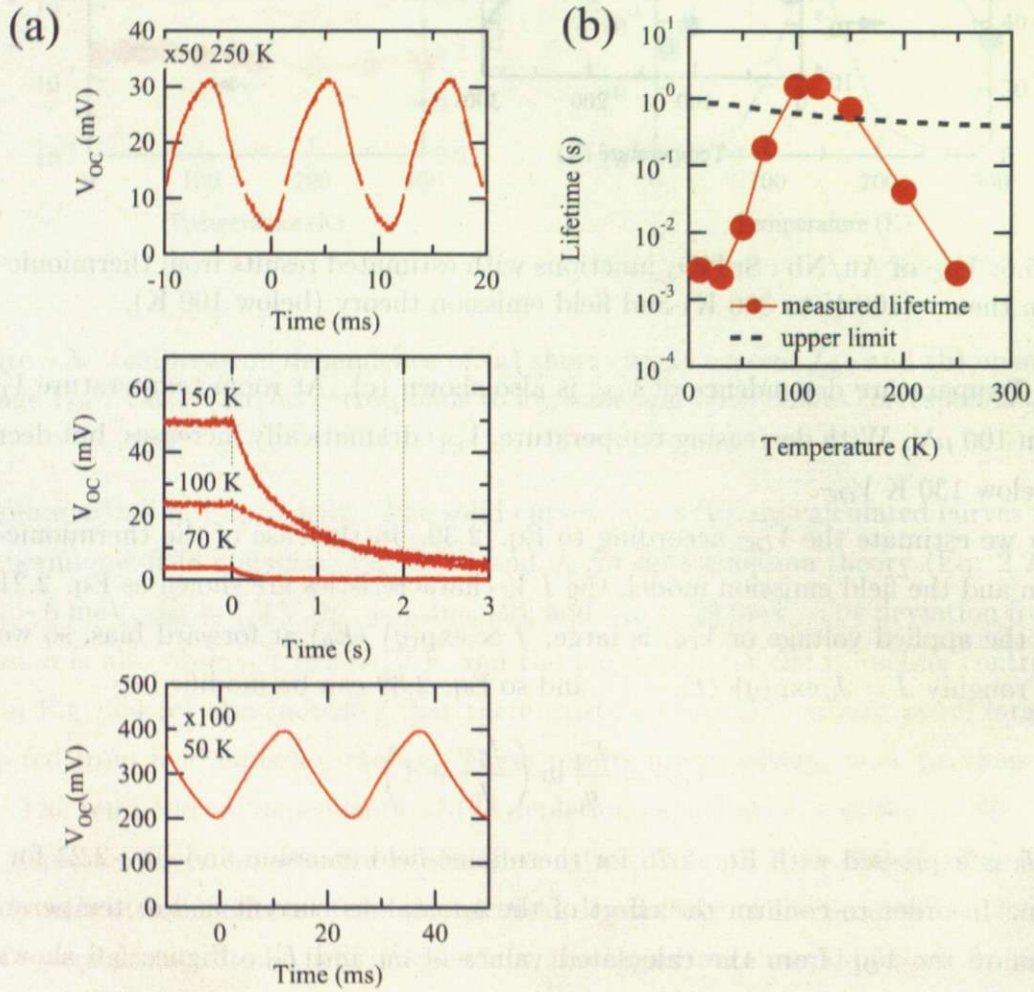

Figure 5.7: (a) Open circuit voltage decay at various temperatures. Voltage was amplified 50-fold at 250 K and 100-fold at 50 K. Optical chopper was used for the measurement at 250 K and at 50 K. For the measurement between 70 K and 150 K, we chopped light by closing the optical shutter manually. (b) Lifetime of stored carriers as a function of temperature. Broken line is upper limit of measurement determined from the junction capacitance and the input impedance of the preamplifier.

lifetime of carriers stored in the depletion layer by single exponential decay. Temperature dependence of the lifetime is shown in Fig. 5.7 (b). In this measurement, samples were connected to a preamplifier with the impedance of 100 $M\Omega$ (Stanford Research system SR560) (Fig. 5.3) The depletion layer capacitance of the sample can be roughly estimated to be 5 nF at all temperatures, which gives a τ_{RC} of about 0.5 s. This sets an upper limit of the measured lifetime. The lifetime of the stored carriers increases with decrease in temperature and exceeds 0.5 s at 150 K. However, below 70 K, the lifetime again decreases with decrease in temperature. This behavior is similar to the temperature dependence of V_{OC}. Lifetime measured with different intensity of irradiation light was almost the same, so lifetime is not determined by the value of V_{OC}. Therefore the reduction of the lifetime of stored charges is the driving force to the reduction of V_{OC}.

Figure 5.8 shows the band diagrams of the Au/Nb : $SrTiO_3$ junctions under light irradiation at low temperature. For (a) we assume the permittivity of the $SrTiO_3$ is constant and for (b) we assume the the barrier sharpening caused by the electric field dependence of the permittivity. Under light irradiation, holes are injected from $SrTiO_3$ to Au. The number of these carriers is expressed with I_{SC}. If the depletion width is large, the tunneling current is small, so the number of electrons injected to Au is small. It is known that the spatial separation of electrons and holes give rise to long lifetime [48], and thus the stored charge also increases and V_{OC} becomes large. However, if the shape of the depletion width is narrow, the tunneling probability is enhanced. Large tunneling current corresponds to the increase of the number of injected electrons in Au. Spatial separation of electrons and holes are reduced and as a result, the recombination rate increases.

5.4 Conclusion

We have studied the electrical properties and the photovoltaic properties of Au/Nb : $SrTiO_3$ from various perspectives and we observed that excess tunneling current caused by the electric field dependent permittivity of $SrTiO_3$ enhances the recombination of injected carriers at low temperature. This induces significant reduction in V_{OC} and the efficiency of photocarrier injection. In order to improve the efficiency of the photocarrier injection, it is necessary to fabricate the structure to reduce this tunneling current by designing heterostructures such as metal-insulator-semiconductor (MIS) structures.

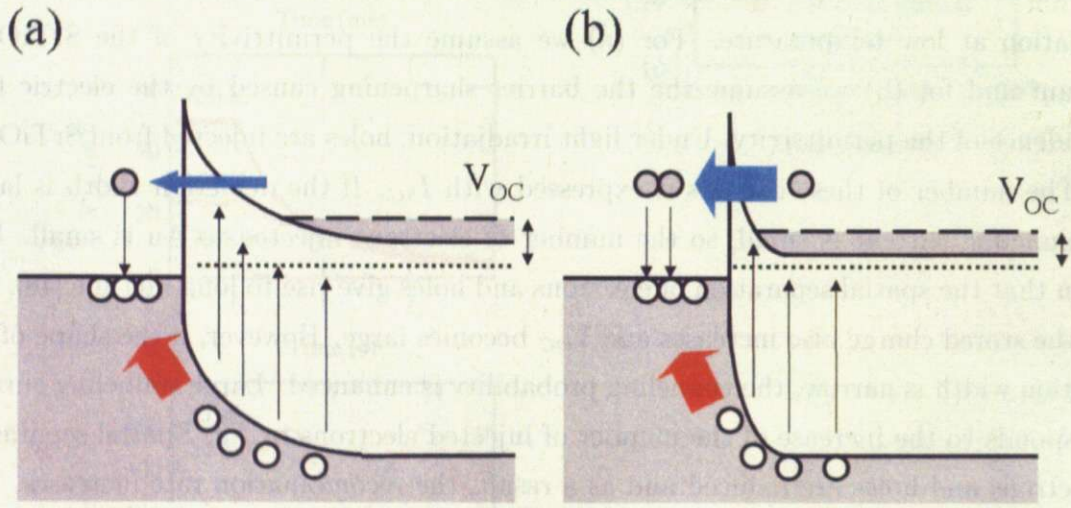

Figure 5.8: Schematic band diagrams of Au/Nb : $SrTiO_3$ junction under light irradiation: (a) without sharpening of band bending (b) including the effect of the field dependent permittivity of $SrTiO_3$ on band bending.